

# SLICK: Strong Lensing Identification of Candidates Kindred in gravitational wave data

Sourabh Magare,<sup>1\*</sup> Anupreeta More,<sup>1,2</sup> Sunil Choudary<sup>3</sup>

<sup>1</sup>*The Inter-University Centre for Astronomy and Astrophysics, Post Bag 4, Ganeshkhind, Pune 411007, India*

<sup>2</sup>*Kavli Institute for the Physics and Mathematics of the Universe (IPMU), 5-1-5 Kashiwanoha, Kashiwa-shi, Chiba 277-8583, Japan*

<sup>3</sup>*The University of Western Australia (M013), 35 Stirling Highway, 6009 Perth, Australia*

Accepted XXX. Received YYY; in original form ZZZ

## ABSTRACT

By the end of the next decade, we hope to have detected strongly lensed gravitational waves by galaxies or clusters. Although there exist optimal methods for identifying lensed signal, it is shown that machine learning (ML) algorithms can give comparable performance but are orders of magnitude faster than non-ML methods. We present the SLICK pipeline which comprises a parallel network based on deep learning. We analyse the Q-transform maps (QT maps) and the Sine-Gaussian maps (SGP-maps) generated for the binary black hole signals injected in Gaussian as well as real noise. We compare our network performance with the previous work and find that the efficiency of our model is higher by a factor of 5 at a false positive rate of 0.001. Further, we show that including SGP maps with QT maps data results in a better performance than analysing QT maps alone. When combined with sky localisation constraints, we hope to get unprecedented accuracy in the predictions than previously possible. We also evaluate our model on the real events detected by the LIGO–Virgo collaboration and find that our network correctly classifies all of them, consistent with non-detection of lensing.

**Key words:** Gravitational Waves – Gravitational Lensing – Machine Learning

## 1 INTRODUCTION

Gravitational waves (GWs) are solutions to Einstein’s field equation in the linearized weak field limit: transverse waves of spatial strain caused by the time variation of the mass quadrupole moment of the source (e.g. Schutz 2009). With the first GW detection of GW150914, by the LIGO detectors at Livingston and Hanford (Abbott et al. 2016), the era of gravitational wave astronomy began. By the end of the third observing run (O3), over 90 events have been detected (e.g. Abbott et al. 2019a, 2021a, 2023a). This also includes GW170817, which was the first coincident detection of GWs and electromagnetic observations from a binary neutron star merger (Abbott et al. 2017a,b). With these detections came an avalanche of discoveries in fundamental physics like the speed of GWs (e.g. Abbott et al. 2017c), constraints on the mass of graviton (e.g. Abbott et al. 2019b), constraints on the violations of lorentz invariance (e.g. Oost et al. 2018; Gong et al. 2018), on violations of equivalence principle (e.g. Wei et al. 2017) and many more (e.g. Miller & Yunes 2019). As the fourth observing run (O4) is ongoing and with the planned future observing runs like O5, Voyager and 3G detectors (e.g. Reitze et al. 2019; Maggiore et al. 2020), which will make the GW detectors even more sensitive, we can expect a flurry of interesting discoveries by the end of next decade.

One of the most anticipated discovery is of observation of gravitationally lensed GWs (e.g. Abbott et al. 2021e). GWs can get lensed if any intervening matter distribution like a galaxy or a cluster is present between the source and the observer (e.g. Gunn 1967; Wang et al.

1996). Gravitational lensing of light is usually described in terms of a simplified framework called the geometric optics where light is treated as rays. However, in case of lensing of GWs, this does not hold true because the wavelength of GW may become comparable to the schwarzschild radius of the lens (e.g. Deguchi & Watson 1986; Nakamura 1998; Takahashi & Nakamura 2003). Thus, the wave-like effects- interference and diffraction- can come into play and one needs to make use of wave optics (e.g. Schneider et al. 1992). When we observe multiple images of the source because of the deflection of light by a massive foreground galaxy or cluster, it is called strong lensing. Just like EM waves, GWs can also get strongly lensed. As the GW signals from the mergers of compact binaries are transient, if they are strongly lensed we will observe identical signals separated by a time delay. In this work, we focus on detection of strong lensing of GW signals.

Till date, only gravitational lensing of EM sources has been observed (e.g. Dai et al. 2020; Hannuksela et al. 2019; Singer et al. 2019; Collaboration et al. 2023; Janquart et al. 2023). Thus, the detection of lensing of GWs in itself can be a testable prediction of general relativity. Currently, gravitational lensing of EM has become a fundamental tool for astrophysics and cosmology. Lensing of GWs can present new avenue to constraint population of galaxies, dark matter distribution, precision cosmography (e.g. Sereno et al. 2011; Li et al. 2019; Jana et al. 2023; Çalışkan et al. 2023c,a), precise test for speed of gravitons (e.g. Fan et al. 2017), tests for gravitational wave polarizations (Goyal et al. 2021a) and detecting intermediate and primordial black hole (e.g. Lai et al. 2018; Oguri & Takahashi 2020; Basak et al. 2022). Particularly, strong lensing can produce multiple images of gravitational wave signal which are separated by

\* E-mail: sourabh.magare@gmail.com

a time delay of minutes to weeks for galaxy. Rapid follow-up of the EM counterpart and the respective constraints can be used to give an early warning of the subsequent counterpart GW signal (Magare et al. 2023). The rates of lensed BNSs and NSBHs, (e.g. Li et al. 2018; Ng et al. 2018; Oguri 2018; Magare et al. 2023), which assume that binary black hole traces star formation rate density, suggest confident detection of strongly lensed gravitational waves within this decade. In future observing runs, we expect to detect very large number of BBH events  $\sim O(10^6)$  in 3G detectors (e.g. Abbott et al. 2021d; Xu et al. 2022), a small fraction of them will be lensed pairs. It is important to identify the lensed pairs without losing accuracy. Efficient, accurate and rapid detection methods are thus needed in the near future.

Neural networks are steadily gaining popularity in the gravitational wave (GW) community. Several research groups have tested the reliability and accuracy of deep learning approaches on glitch classification, gravitational wave detection and parameter estimation (e.g. George et al. 2018; Bahaadini et al. 2017; Shen et al. 2019; Cavaglia et al. 2019; Goyal et al. 2021b). Some recent studies have demonstrated that CNNs could be used for identifying gravitational lenses using images of the lensed galaxies (e.g. Jaelani et al. 2023; Jacobs et al. 2017, 2019; Li et al. 2021; Zaborowski et al. 2023). The real advantage of using a machine learning algorithm is that the only computationally expensive task is the training period of the neural network and is to be done only once. The evaluation time of any neural network on a sample data tends to be orders of magnitude faster than any other technique (Smith et al. 2016). We believe that the speed of machine learning algorithms can be of great utility for identifying strongly lensed pairs of GW signals provided accuracy is not compromised. The multiple copies of GW signal are separated by the time-delay and can have different amplitudes, however their phase evolution is expected to be identical for non-spinning circular binaries (e.g. Haris et al. 2018; Dai & Venumadhav 2017). Thus, one way to infer, whether the given pair of signals are lensed or not, is by comparing the inferred posteriors on the intrinsic parameters. Strongly lensed pairs will show large overlap while unlensed signals will not show any significant overlap. The way to quantify this comparison is using bayesian model selection (e.g. Haris et al. 2018; Hannuksela et al. 2019; Goyal et al. 2021b; Janquart et al. 2022b; Çalıřkan et al. 2023b; Cheung et al. 2023). Given a pair of signal, calculate the bayes factor which is defined as the ratio of evidences of joint data of both signals. However, this is time consuming and computationally expensive. Bayesian parameter estimation of a BBH signal can take several hours to days. The situation gets worse, for example, we expect  $O(100)$  BBH events in O4 observing run and this number increases greatly for future observing runs (e.g. Abbott et al. 2021d). Like for O5 and voyager, number of BBH events is estimated to be of  $O(10^3) - O(10^4)$ , while for the 3G observing run, this number will likely be  $O(10^6)$ , out of which only a small percent could be strongly lensed (e.g. Xu et al. 2022). Thus, bayesian model selection technique may not be as efficient and fast for growing number of events. There are alternative pipelines e.g. GOLUM (Janquart et al. 2022a), HANABI (Lo & Magaña Hernandez 2023) and phazap (Ezquiaga et al. 2023). GOLUM is a faster technique to estimate joint parameters for a pair of events. HANABI takes in consideration the astrophysical information and selection effects, and uses hierarchical analysis for efficient computation of probabilities. phazap exploit the fact that phases are the best measured GW quantities and construct a joint distance which is a measure confidence level of lensing hypothesis for a pair of events. However, in terms of computational speed, these algorithms may take  $O(30)$  minutes –  $O(\text{hours})$  for an event pair. Lower latency and complementary techniques are still desirable

if we are expecting  $O(10^3) - O(10^4)$  events which machine learning algorithms could facilitate.

Goyal et al. (2021b, henceforth referred to as G21) applied deep leaning algorithm on Q-transform maps (QT maps, Chatterji et al. 2004) and sky localisation maps (skymaps, Singer & Price 2016) for identifying strongly lensed pairs. Their injections are added in gaussian noise. Further, the data is prepared such that a pair of (un)lensed events are superposed. Since random pair of events will have distinct projections in QT whereas lensing implies similar intrinsic parameters, the superposed maps will show differences between the lensed and unlensed pairs. However, we find that such QT maps can result in many false positives i.e. unlensed pairs getting classified as lensed. This is possible when the signal-to-noise ratio (SNR) of one event is sufficiently contrasting to the SNR of another event in the pair. In this work, we attempt to bypass this issue by using QT maps along with the Sine Gaussian Maps (SGP-maps Choudhary et al. 2023). We find that using both representations increases the efficiency in identifying lensed pairs as compared to QT maps alone. Further, to improve the robustness of our network, we train with a dataset consisting of injections in real noise as well as in gaussian noise and compare their performance.

The rest of the paper is organized as follows. In Sect. 2, we describe the type of input data used, sample preparation, suitability of data for binary classification, the neural network models that are developed for the Strong Lensing Identification of Candidates Kindred (SLICK) pipeline. Sect. 3 describes our results on various datasets including the comparison with the previous work by G21. Sect. 4 gives the summary of our work.

## 2 METHODOLOGY

The SLICK pipeline is designed to take simulated or real GW signals, generate input data in the form of images and run a custom neural network to predict whether a pair of signals are strongly lensed or not. We describe below the components of the SLICK pipeline along with the methodology.

### 2.1 Input Data Representation

We use two type of data representations - QT Maps and SGP Maps.

The Q-transform (Chatterji et al. 2004) technique has long been used as a visualization tool in the LIGO–Virgo data analysis. It is a modified short-time fourier transform where the analysis window duration varies inversely with frequency such that the plane of time-frequency is covered by the tiles of constant  $Q$ . The continuous Q-transform is given by

$$x(\tau, f) = \int_{-\infty}^{\infty} x(t) w(t - \tau) \exp(-2\pi i f t) dt \quad (1)$$

where  $w(t - \tau, f)$  is a window function centered at  $\tau$  and depends on the quality factor  $Q$ ,

$$Q = \frac{f}{\delta f} \quad (2)$$

The discrete version of the above is more appropriate for gravitational wave data, as this data is collected in discrete time bins,

$$x[m, k] = \sum_{n=0}^{N-1} x[n] w[n - m, k] \exp(-2\pi i n k / N) \quad (3)$$

The value of  $Q$  is set in the following way: When we perform Q-transform of a signal, we have to specify a range of values of  $Q$ . The

value of  $Q$  which corresponds to the largest SNR is chosen. This transformation creates a tile in time and frequency domain and the value in each tile corresponds to the energy of the signal. The Fig. 1 shows the QT map (bottom) of a BBH merger event.

The other kind of data representation, we use, is called the SGP maps (Choudhary et al. 2023). It is mathematically expressed as

$$g(t) = A \exp\left(-4\pi f_0^2 \frac{(t - t_0)^2}{Q^2}\right) \cos(2\pi f_0 t \phi_0) \quad (4)$$

where  $A$  is the constant amplitude,  $Q$  is the quality factor,  $f_0$  is the central frequency,  $\phi_0$  is the phase and  $t_0$  is the central time. Let  $x(t)$  be the timeseries data, then the projection of timeseries data on the sine-Gaussian is given by

$$(x, g) = 4\text{Re} \int_{f_{\text{lower}}}^{f_{\text{higher}}} \frac{\tilde{x}^*(f) \tilde{g}(f)}{S_n(f)} df \quad (5)$$

where  $S_n(f)$  is the power spectral density (PSD) of the noise and  $\tilde{x}(f)$  and  $\tilde{g}(f)$  are the fourier transform of the  $x(t)$  and  $g(t)$ , respectively.

For constructing the SGP maps, we evaluate the above projection in the space of  $f_0$  and  $Q$ . The chosen range of  $f_0 \in [20, 240]$  Hz and  $Q \in [2, 80]$ . The Fig. 1 shows the SGP map (top) of a BBH merger event.

From the QT and SGP maps of an event pair, we look for features that can help us discern a lensed pair from an unlensed pair. Usually the lensed events are a pair of events which have the same intrinsic parameters like mass and spins but with different amplitudes (e.g., Schneider et al. 1992; Takahashi & Nakamura 2003; Dodelson 2017). This implies that the pair of lensed signals should have mostly similar projections in the QT as well as SGP maps modulo some differences from extrinsic parameter and arrival times. However, a random pair of unrelated signals are less likely to have similar intrinsic parameters and thus, their QT and SGP maps are not expected to be strongly similar. Such similarities will only rarely occur by chance.

In Fig. 2 and Fig. 3, we show the input data representations of lensed and unlensed images. For the QT maps per event pair as input data, we choose a  $2 \times 1$  grid format where a row corresponds to the detector (H1 or L1) and each map is a superposition of the pair of events. It is clear from Fig. 2, that the lensed events have similar projections and near perfect overlap while the maps of the unlensed event pairs do not have as much overlap. This serves as the primary distinguishing criterion between the lensed and unlensed event pairs. For the SGP maps of an event pair, we choose a  $2 \times 2$  grid format instead. Here, each row corresponds to each event in the pair while each column corresponds to each detector, H1 and L1. It is clear from the Fig. 3 that for the lensed pair, higher projections are seen in the same region of the  $Q - f_0$  plane, while the unlensed event pair may not have similar projections. As before, these patterns help distinguish the lensed pair from the unlensed ones.

## 2.2 Image classification problem

We see from Fig. 2 that for the QT maps, superposed lensed pair of events show different morphological features than superposed unlensed pair of events. The lensed pair has different amplitudes but similar time evolution since their intrinsic parameters are the same, while the unlensed pair, in general, will have distinct intrinsic parameters. These make their morphologies distinct. Thus, the problem of identifying the lensed and unlensed pairs can be framed as a binary image classification problem, and can be well handled by Deep Learning networks (Schmidhuber 2015).

Since the lensed pairs will have identical frequency evolution, we

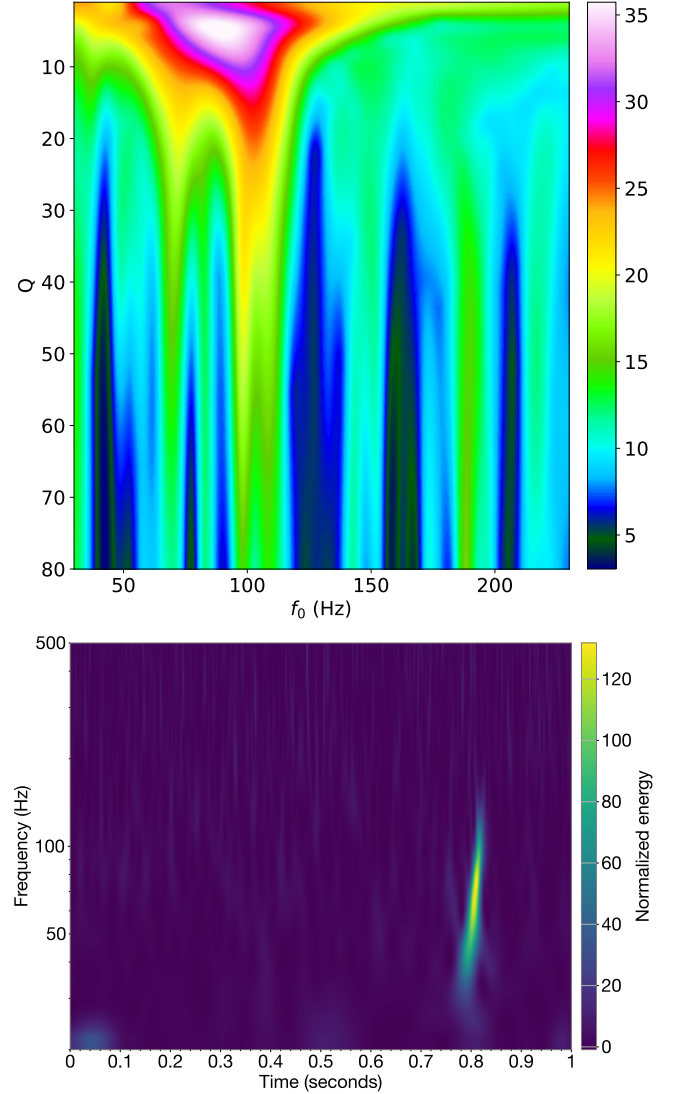


**Figure 1.** *Top:* Sine-Gaussian projection (SGP) map of a simulated BBH signal injected in gaussian projected O4 noise. The color represents the value of the projection of the timeseries data on the sine-gaussian function. *Bottom:* Q-transform map of a BBH signal injected in gaussian noise. The color represents the normalized energy of the signal.

should expect that the projection of signal in the  $Q - f_0$  plane of the SGP should be identical. Our expectations are validated from Fig. 3. The lensed pair is projected on the identical part of the  $Q - f_0$  plane while a randomly selected unlensed pairs is projected on different parts of this plane. In case of SGP maps input data, we haven't superposed the pair of signals, but rather kept them as  $2 \times 2$  tiles. We expect that the SGP maps provides the complementary information to QT maps and together with QT maps will help reduce the false positives.

## 2.3 Generation of Sample

We prepare the timeseries data by injecting a simulated GW signal in real and gaussian noise. We follow More & More (2022) to generate lensed and unlensed populations of binary black holes (BBHs). We consider the mergers of BBHs as the background source and massive

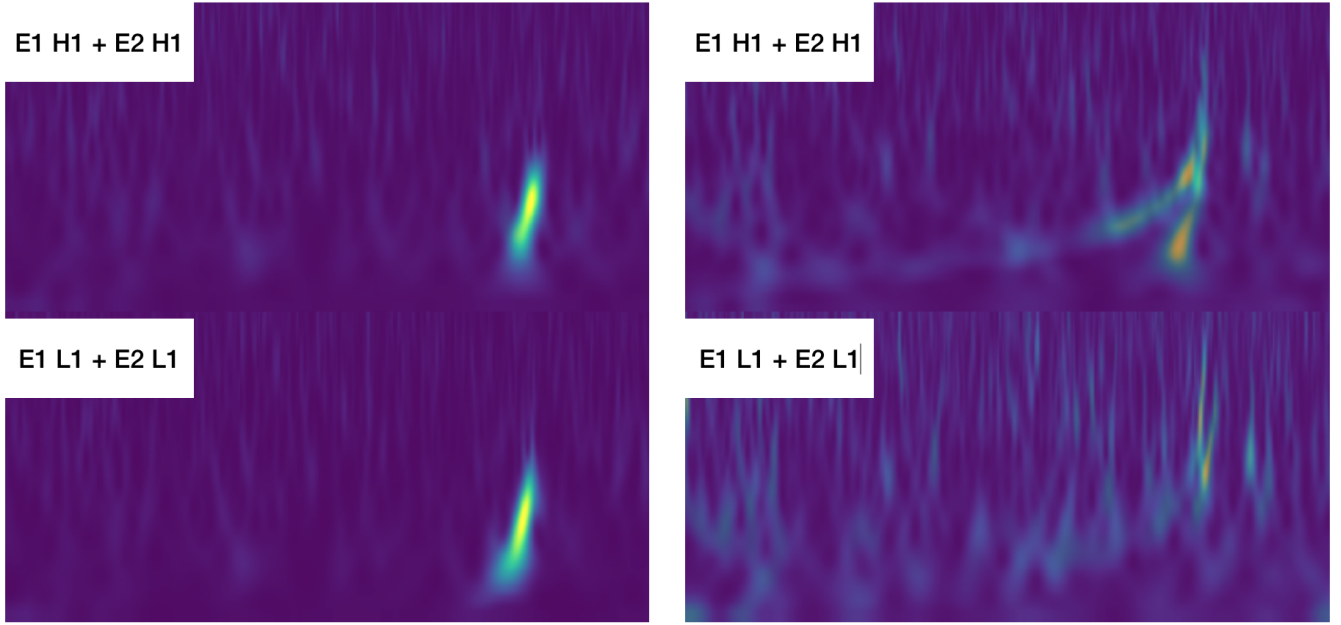


**Figure 2.** Sample format of input data to the neural network that analyses the QT maps. The QT maps for a pair of events (E1 and E2) are superposed and the QT maps from two detectors (H1 and L1) of the corresponding events are placed one below the other. *Left:* Sample QT maps for a lensed event pair. *Right pair:* Sample QT maps for an unlensed event pair.

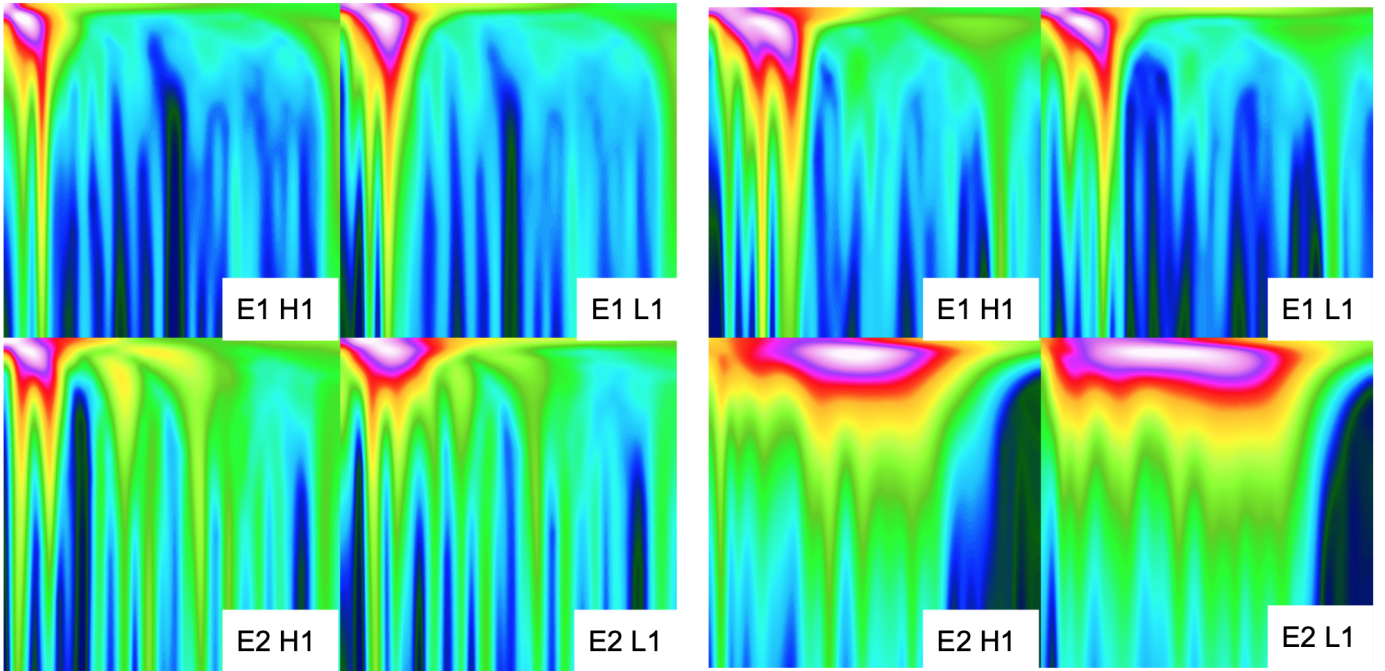


**Figure 3.** Sample format of input data to the neural network that analyses SGP maps. The SGP maps are produced in a 2x2 grid format where the labels imply the following - E1H1: Event1 in H1 detector, E2H1: Event2 in H1 detector, E1L1: Event1 in L1 detector, E2L1: Event2 in L1 detector. *Left:* Sample SGP map for a lensed event pair. *Right:* Sample SGP map for an unlensed event pair.

early type galaxies as the lens galaxies. The density profile of the galaxies is given by a Singular Isothermal Ellipsoid (SIE) lens model (Kormann et al. 1994). The SIE model produces either two lensed images (double) or four lensed images (quad). In case of a quad, we choose the brightest two images to define a lensed pair such that the fainter event in the pair has a network SNR  $> 8$ . The same SNR condition is applied to a double.

We generate  $\approx 17000$  lensed pairs and  $\approx 4000$  unique unlensed events. We then divide this set into training, validation and testing samples. For training, we use 12000 lensed pairs and make random pairs from the catalog of unlensed events, to get 12000 unlensed pairs. Similarly, we prepare a sample of 2000 each of lensed and unlensed pairs for the validation sample. We use the remaining samples as the test sample. We use the IMRPhenomPv2 (e.g. Hannam et al. 2014; Khan et al. 2016) waveform approximant, implemented in LALSuite, to generate the simulated GW signal. We take into account the antenna patterns from the two LIGO detectors, Livingston (L1) and Hanford (H1), to produce the final ‘‘observed’’ signal, before adding the noise, using the PyCBC package. While generating the lensed signals, we also apply the morse phase shift to the type II images (saddle points). The morse phase for both the doubles and typically, the two brightest images of the quad are  $\frac{\pi}{2}$ . Although, we do not expect that the phase shift effects will manifest in either the QT maps or the SGP maps.

We train and test the neural networks on gaussian as well as real detector noise which are referred to as Dataset-G and Dataset-R, respectively (see Table 1). To generate the Dataset-G, we use the aLIGO PSDs<sup>1</sup> to produce 16-sec-long  $\approx 21\,000$  unique noise segments and inject our simulated signals in them. To generate the Dataset-R, we extract a 60-min data segment from the third observing run (O3) of LIGO-Virgo (Abbott et al. 2021c, 2023b). This serves as our parent noise data chunk from which again  $\approx 21\,000$  unique noise segments are extracted with a random start-time. The simulated signals are then injected in these 16-sec-long real noise segments.

Further, we also evaluate the performance of our neural network on real events detected in O2 and O3 called the Dataset-LHV (Abbott et al. 2019a, 2021b, 2023a). We take 8 events from O2: between GW170104 to GW170823, and 36 events from O3: between GW190408 to GW180930. We pair these events with each other to obtain a total of 1035 pairs. We assume that all of the real event pairs are unlensed and evaluate the neural network based on the mis-classification of these unlensed pairs as lensed.

To generate the QT maps, we use the Q-transform method in GWPY package on the timeseries data. In the Q-transform method, we choose the *frange* = [20, 512] and also set the *whiten* parameter to be true. We chop the timeseries to a length of 1 second with the peak of the merging signal to be located at 0.8 s. We set the frequency from 30 Hz to 1000 Hz and  $q = (4, 64)$ . The same timeseries is then used to generate the SGP maps. For generating the SGP maps, we choose the range of  $f_0 \in [20, 240]$  Hz and  $Q \in [2, 80]$ . The data points in the chosen range are then sampled uniformly and for each data point, the time series is projected on the Sine Gaussian function using Eq. 5. This projection is then presented using a color map and spline interpolation is used for smoothing of pixels.

## 2.4 Deep Learning Models

In this section, we give a brief description about the neural networks that are used in the SLICK pipeline. The readers may refer to LeCun

**Table 1.** Description of various datasets used in our analysis

Dataset	Description
G	Simulated GW signals are injected in <b>gaussian</b> noise which is generated using Advanced LIGO PSDs.
R	Simulated GW signal are injected in <b>real</b> noise. These noise segments are extracted from O3 run for H1 and L1 detectors.
LHV	Detected events from O2: between GW170104 and GW170823 and O3: between GW190408 and GW180930. Total 46 events which gives 1035 pairs.
DST	BBH parameter samples used by G21. Using these samples, GW signals are simulated and injected in <b>gaussian</b> noise which is generated using Advanced LIGO PSDs.

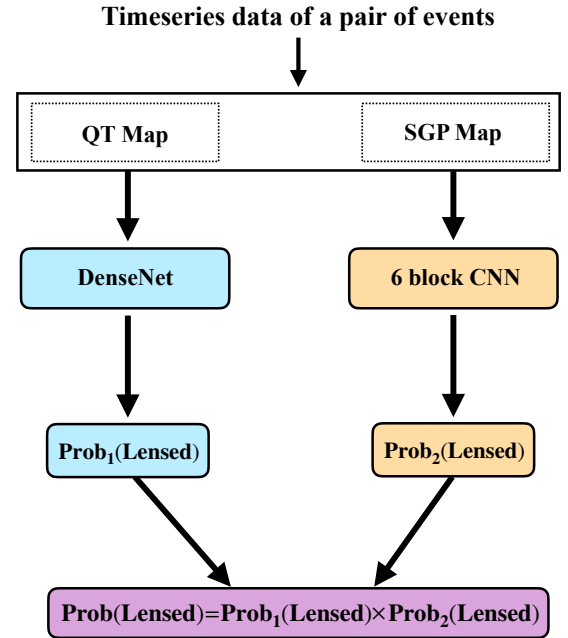


**Figure 4.** Visual representation of the workflow of SLICK. Using the timeseries data for a pair of events, QT and SGP maps are generated. These maps serve as input data through their respective neural network models where the output from each network is a probability for the pair of events to be lensed. The final output of our SLICK pipeline is a combined probability.

et al. (2015) and Schmidhuber (2015) for a detailed review on deep learning.

A specialized class of deep neural network, which have been proven highly effective in computer vision task like image recognition are the Convolutional Neural Networks (CNNs, e.g. Huang et al. 2018; Krizhevsky et al. 2012; LeCun et al. 2015). CNNs typically have the following structure- Convolutional layers, Pooling layers and Fully connected layers. Convolutional layers perform the convolution operation-which involves the sliding a matrix called filter or kernel over the input to perform element-wise multiplication to generate output which is called a feature map or activation map. Pooling layers are also known as downsampling, which performs

<sup>1</sup> <https://dcc.ligo.org/LIGO-T2000012/public>

**Table 2.** Various types of network models and datasets used therein.

Model	QT maps Training	SGP maps Training
Model-Q <sub>r</sub>	Dataset-R	-
Model-Q <sub>r</sub> S <sub>g</sub>	Dataset-R	Dataset-G
Model-Q <sub>r</sub> S <sub>r</sub>	Dataset-R	Dataset-R

dimensionality reduction-i.e. to reduce the spatial dimensions of the feature map while also retaining relevant information. Max pooling and Average pooling are the two commonly used pooling layers. After many blocks of convolutional layers followed by pooling layers, a typical CNN ends with fully connected layers. Here, each node in a layer is connected to every node of the previous layer. These layers perform the classification based on the extracted features from the convolutional layers.

We build two independent ML models- one that learns from QT maps and other learns from SGP maps for binary classification of lensed and unlensed pairs. First network is the Densenet121 model that is trained on the superposed QT maps. The Fig. 2 shows the input image data given to this neural network. The second network is a standard CNN model which consists of 6 convolution blocks and is trained on the SGP maps. The Fig. 3 shows the input data given to this network. The outputs of both these networks are combined to get the final probability that the given pair of events are lensed or unlensed. Fig. 4 shows a graphical representation of the overall workflow.

*DenseNet121:* DenseNet (Densely Connected Convolutional Networks) are deep convolutional networks in which each layer receives direct inputs from all preceding layers-these are called dense connections (Huang et al. 2018). Using this design they reduce the problem of vanishing gradients, enhance feature propagation and reduce the number of parameters. DenseNet121 refers to a specific architecture with 121 layers. However, it is still difficult to train this neural network from scratch, thus we make use of transfer learning. Transfer learning is a technique where a network which is trained for a particular task is reused for a different but related task (e.g. Yosinski et al. 2014). For our binary classification problem of distinguishing between lensed and unlensed images, we use DenseNet121 model which is pre-trained of ImageNet dataset (Deng et al. 2009). We make some changes to the network like adding new fully connected layers along with Dropouts after the DenseNet121 model. We then set the first 10 layers to be non-trainable. Densenet121 is used on the QT maps to distinguish between lensed and unlensed events. We train this network on 12000 lensed and 12000 unlensed pair QT maps of *Dataset-R* as described in section 2.2.

*6-CNN model:* We use a 6-CNN layered network on the SGP maps to distinguish between lensed and unlensed pair of events. Fig. 5 shows the detailed network architecture of this model. We train this network from scratch on 12000 lensed and 12000 unlensed pairs of SGP maps of two different datasets- *Dataset-G* and *Dataset-R*.

After training DenseNet and CNN model individually, we combine output of both to get the final probability that the given pair of events are lensed or unlensed, as shown in the workflow Fig. 4. We name the networks with respect to their training dataset as shown in the Table 2.4.

The nomenclature adopted is as follows: for Model-Q<sub>α</sub>S<sub>β</sub>, the QT maps part of the network (*DenseNet121*) is trained on dataset-*α* and the SGP part of the network (*6-CNN*) is trained on dataset-*β*.

For Model-Q<sub>r</sub>, there is no SGP-map part of the network, so ‘S’ is ignored from its name.

### 3 RESULTS AND DISCUSSION

We assess the performance of the trained models by evaluating them on various test datasets. We use the Receiver Operating Characteristic (ROC) curves as a statistic of comparison between different trained models. The ROC plot describes a trade off between the true positive rate (TPR, y-axis) and false positive rate (FPR, x-axis). The TPR is the ratio between the correctly classified lensed events to the total number of lensed events, while the FPR is the ratio between incorrectly classified unlensed events to the total number of unlensed events. The ideal ML model should have a TPR and a FPR as 1 and 0, respectively, at all thresholds.

Firstly, we compare the performance of our ML models with the work of G21. We use the DST dataset on which the G21 network is evaluated. For convenience, we work on a subsample of DST dataset that includes 300 pairs of lensed events and 30,000 pairs of unlensed events. We further test our model on a sample of randomly selected lensed and unlensed pairs with the same ratio from our Dataset-G (see Fig. 6). For comparison, we also plot the ROC curve of G21, which is evaluated on the QT maps of the Dataset-DST. We see that both the Model-Q<sub>r</sub> and Q<sub>r</sub>S<sub>g</sub> are performing better than G21 at lower FPRs ( $< 10^{-3}$ ). Further Model-Q<sub>r</sub>S<sub>g</sub>, trained on both the QT maps and the SGP maps, performs better compared to the Model-Q<sub>r</sub>, trained only on the QT maps.

Next, we create larger test datasets of different kinds and compare their performances with each other along with results of G21 (see Fig. 7). We evaluate the performance of our ML models on a test sample extracted from Dataset-G. Here, we take 2000 lensed pairs and 100,000 unlensed pairs. All of our models perform better than G21 even on this larger dataset (see *top left panel* of Fig. 7). Further, to compare between our own models, we find that Model Q<sub>r</sub> S<sub>g</sub> (solid black) performs better than Q<sub>r</sub> (solid orange) demonstrating the importance of including constraints from SGP maps. Also, since the Model Q<sub>r</sub> S<sub>g</sub> (i.e. the network trained on QT maps from Dataset-R and SGP maps from Dataset-G) performs marginally better than Q<sub>r</sub> S<sub>r</sub>. Hence, we choose Q<sub>r</sub> S<sub>g</sub> as our final best network model. We further find that the Model Q<sub>r</sub> performs better on the QT maps test dataset made with Gaussian noise (dash-dotted orange) as compared to the real noise (solid orange).

Subsequently, we divide this dataset based on their signal-to-noise ratio (SNR), total mass ( $M_t$ ) and mass ratio ( $q$ , with  $0 < q \leq 1$ ). If the network SNR of both of the events in a pair is between 10 and 15 then its called high SNR while if the network SNRs of either of the events are  $\leq 10$ , then this pair is considered as low SNR. High- and low- total mass (detector frame mass) correspond to  $> 80 M_\odot$  and  $\leq 80 M_\odot$ , respectively. And, high- and low- mass ratio correspond to  $q > 0.6$  and  $0.3 < q < 0.6$ , respectively. Here, we compare performances of Models Q<sub>r</sub> S<sub>g</sub>, Q<sub>r</sub> S<sub>r</sub> and Q<sub>r</sub>. From the Fig. 7, we can infer that the Model-Q<sub>r</sub>S<sub>g</sub> (black) is almost always better than the other models, more so at lower FPRs.

As expected, our models perform better on high SNR (dashed) as compared to low SNR (dotted) shown in the *top right panel* of Fig. 7. In case of high- and low-  $M_t$ , we find that our models perform better on high  $M_t$  as compared to low  $M_t$ . And, in the case of high- and low-  $q$ , our models have better performance on low  $q$  than on high  $q$ .

Lastly, we test our models on the real events detected by the LIGO–Virgo collaboration. Here, we use the Dataset-LHV (see Table 1) which contains 46 real events during O2 and O3. We pair each event

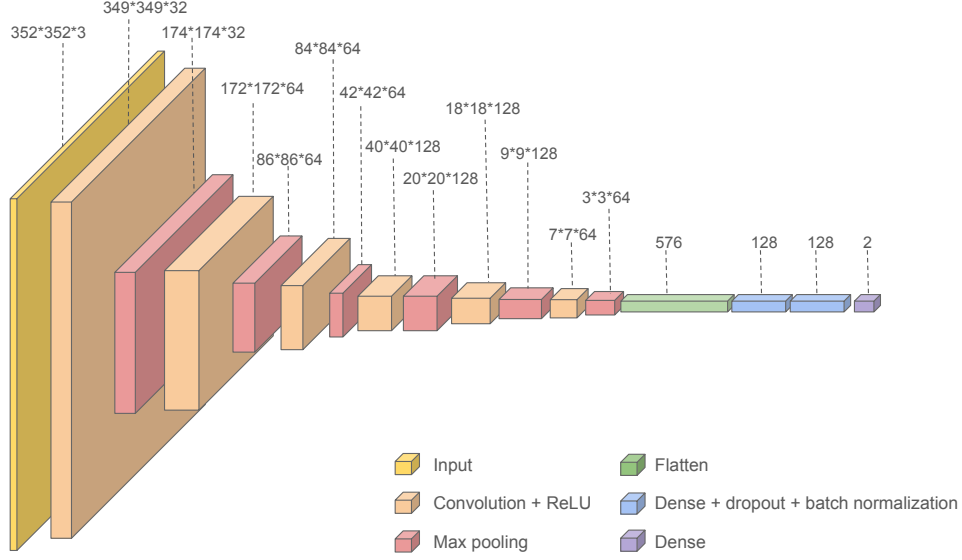


**Figure 5.** The 6 block CNN model used for classification of lensed and unlensed pairs with the SGP maps as input data.

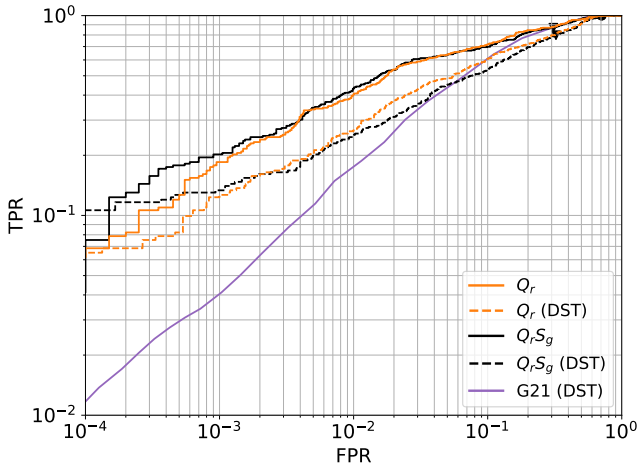


**Figure 6.** Evaluation of our models on Dataset DST and our datasets along with the comparison of results from G21. We choose 300 lensed pairs and 30,000 unlensed pairs from each of the dataset for a fair comparison. The Model- $Q_r S_g$  (solid black curve), comprising QT and SGP maps, performs well at low FPRs as compared to the Model- $Q_r$  (orange curve), with QT only data, tested on both DST and our datasets.

with every other, this gives us a total of 1035 pairs. We evaluate the Model- $Q_r S_g$  on this dataset assuming all of the 1035 event pairs are unlensed. As a metric, we plot the fraction of mis-classifications as a function of the network threshold which is the lower bound on the output probability of the network to consider an event pair to be lensed (see Fig. 8). Since the Model- $Q_r S_g$  has two parallel networks one trained on the QT maps and the other on the SGP maps. In Fig. 8, we also show the fraction of mis-classifications for Model- $Q_r$  (orange) and Model- $S_g$  (brown) along with their combined output probability (black). This further demonstrates that the Model- $Q_r$  or  $S_g$  alone has a higher number of mis-classifications whereas the combined Model- $Q_r S_g$  gives a drastically lower number of mis-classifications.

During our analysis, we noticed that superposition approach in the

preparation of QT maps may be prone to producing more FPs. For instance, consider event 1 of the pair has a very high SNR and the event 2 has a low SNR (but still super-threshold) which are not lensed. The QT map of event 1 will show clear chirping signal, while the QT map of event 2 will be mostly noise-like because of the low SNR. When superposed, the resulting image is dominated by the stronger event 1. This mimics the appearance of a superposed lensed pair and will be classified as a lens even though the events are unlensed in reality. However, the  $2 \times 2$  grid chosen for SGP maps is less likely to result in FPs as is evident from Fig. 8.

#### 4 SUMMARY

The current method to infer the probability for a pair of GW signals to be lensed is by comparing the posteriors of the intrinsic parameters. Lensed pairs will have large overlap in the posteriors while the unlensed pairs will not show significant overlap and the comparison is quantified using bayesian model selection referred to as the posterior overlap method. However, this technique is time consuming and can take hours to days for parameter estimation. There are also some alternative pipelines- GOLUM, HANABI and phazap. However, in terms of computational speed, these algorithms may take  $\mathcal{O}(\text{hours})$  for an event pair. Further, in the future observing runs, such as O5 and voyager, the predicted number of detectable events are  $\mathcal{O}(10^3) - \mathcal{O}(10^4)$ , and for the 3G detectors, the predicted numbers are  $\mathcal{O}(10^6)$ . Thus, the posterior overlap and other methods may be computationally expensive relative to machine learning algorithms. These pipelines could nevertheless serve as complementary techniques and could possibly be applied on the candidates selected by ML algorithm such as SLICK.

In SLICK, we use two neural network models - *Densenet121* and *6 block CNN*, which are trained on the QT maps and SGP maps, respectively. The output from these two models is then combined to give a final output probability which tells whether the given pair of events is lensed or not. We work with 3 datasets - 1) GW signals injected in stationary gaussian O4 noise (Dataset-G), 2) GW signals injected in real O3 noise (Dataset-R) and 3) real GW events (Dataset-

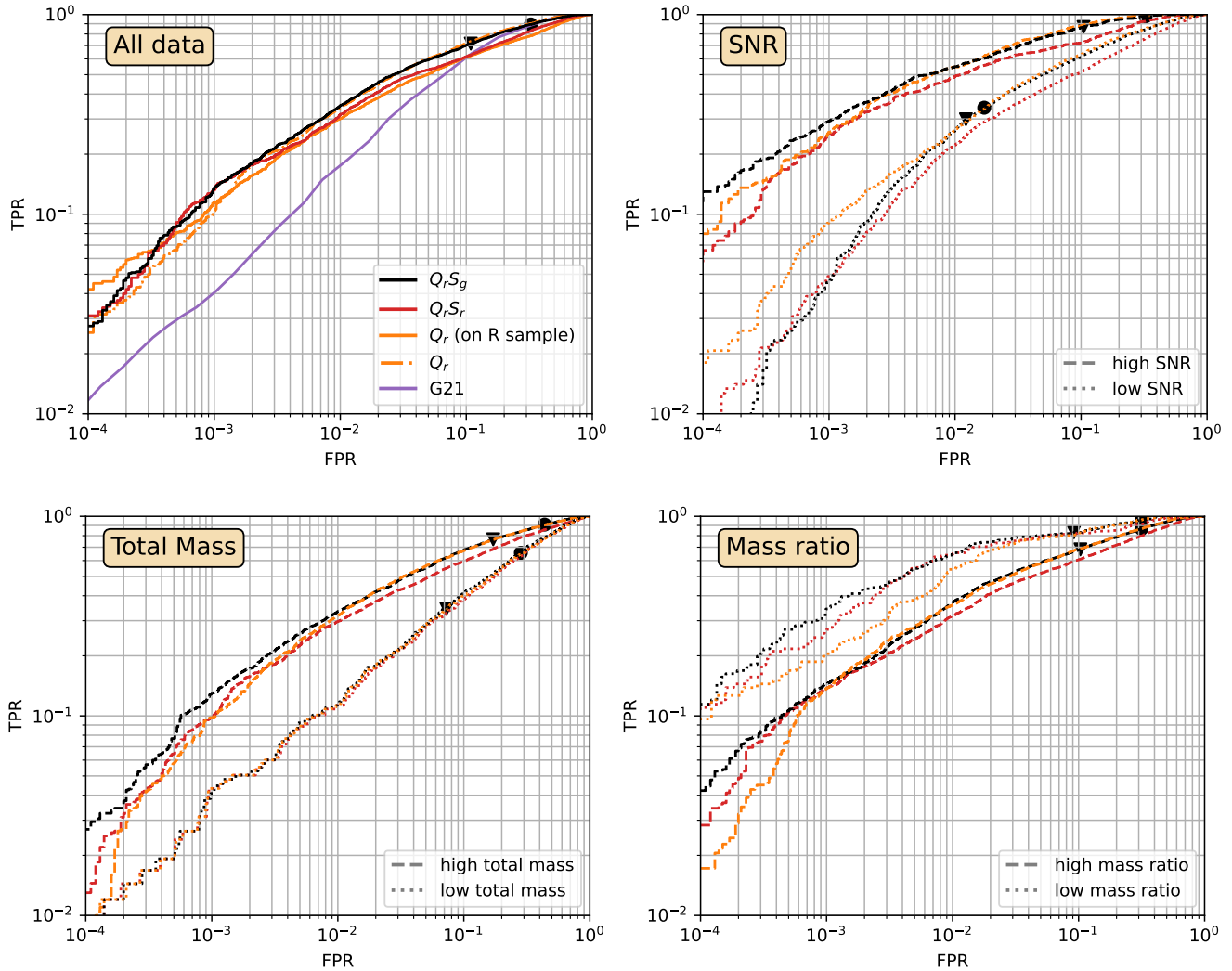


**Figure 7.** Performance of our networks on test samples made from Dataset-G. *Top left panel:* The “All Data” consists of 2,000 lensed pairs and 100k unlensed pairs. Here, we find that the hybrid trained model (solid black curve) performs better than QT only model especially (solid red curve) at low FPRs. The Model- $Q_r$  is tested on both Dataset-G (dashed-dotted orange) and Dataset-R (solid orange) with the former performing moderately better. We then create a subsample of the “All Data” as a function of SNR (*top right panel*), total mass (*bottom left panel*) and mass ratio (*bottom right panel*). These subsamples are then divided in high and low bins (e.g. high and low snr). Here, the *dashed* correspond to ROCs at high values (e.g. high snr) and the *dotted* correspond to ROCs at low values (e.g. low snr). The *black triangle* and *black circle* correspond to 0.9 and 0.7 probability, respectively.

LHV). We use the first two datasets for training, validation and testing whereas the third dataset is for testing only. The networks are trained on different datasets to create 3 different “best” models which are labelled as Model- $Q_r$ , Model- $Q_r S_g$  and Model- $Q_r S_r$  where Q and S refer to the type of data (QT or SGP maps, respectively) and the subscript r or g correspond to the training dataset based on the type of noise.

Firstly, we test our models on the QT maps prepared from the same BBH sample as G21 (DST dataset) and compare the ROC curves. We find that Model- $Q_r$  has an improved performance, especially, at lower FPRs ( $< 0.01$ ). We also infer that Model- $Q_r S_g$  performs better than Model- $Q_r$ . Our inference does not change when we evaluate our models on our test datasets. Our models, when tested, on real GW events strengthens the confidence in Model- $Q_r S_g$  further as it significantly reduces misclassifications compared to models that use either QT or SGP data alone. Thus, the final best model of SLICK is chosen to be Model- $Q_r S_g$ .

We note that sky localisation is expected to provide strong constraints for lensed event pairs (also, demonstrated by G21). Thus, including skymaps as additional type of input data in SLICK will further improve its performance. However, it is not imperative to include it in the machine learning framework since skymaps can also be easily used as a screening step subsequently on the promising candidates.

In the future, we plan to include signals with added complexities such as spinning/precessing and eccentric BBH signals. It will be interesting to see if SLICK can continue to give robust predictions with high efficiency allowing us correctly classify a broader sample of GW signals.



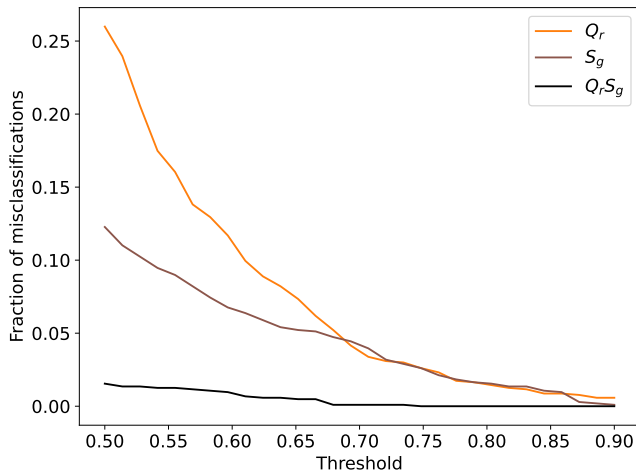


**Figure 8.** Fraction of misclassifications of Dataset LHV as a function of network threshold. Evaluation is done on a total of 46 events resulting in 1035 pairs where all of the events are assumed to be unlensed. We can see a drastic improvement in the mis-classification when combined QT and SGP data representation (black curve) is used as opposed to using only single data representation of either QT (orange) or SGP (brown).

## ACKNOWLEDGEMENTS

We would like to thank Soorya Narayan, Sudhagar S, Srashti Goyal and Shasvath Kapadia for useful discussions. We acknowledge the use of IUCAA LDG cluster Sarathi for the computational/numerical work. This material is based upon work supported by NSF’s LIGO Laboratory which is a major facility fully funded by the National Science Foundation. This work uses NumPy (Harris et al. 2020), SciPy (Virtanen et al. 2020), Pandas (Wes McKinney 2010), PyCBC (Nitz et al. 2024), GWpy (Macleod et al. 2021), LALSuite (LIGO Scientific Collaboration et al. 2018), TensorFlow (Abadi et al. 2015) software packages.

## DATA AVAILABILITY

The SLICK pipeline and the data used in the training and testing will be available upon reasonable request to the authors.

## REFERENCES

Abadi M., et al., 2015, TensorFlow: Large-Scale Machine Learning on Heterogeneous Systems, <http://tensorflow.org/>  
 Abbott B. P., et al., 2016, *Phys. Rev. Lett.*, 116, 061102  
 Abbott B. P., et al., 2017a, *Phys. Rev. Lett.*, 119, 161101  
 Abbott B. P., et al., 2017b, *The Astrophysical Journal Letters*, 848, L12  
 Abbott B. P., et al., 2017c, *The Astrophysical Journal Letters*, 848, L13  
 Abbott B. P., et al., 2019a, *Phys. Rev. X*, 9, 031040  
 Abbott B. P., et al., 2019b, *Phys. Rev. D*, 100, 104036  
 Abbott R., et al., 2021a, *Phys. Rev. X*, 11, 021053  
 Abbott R., et al., 2021b, *Physical Review X*, 11  
 Abbott R., et al., 2021c, *SoftwareX*, 13, 100658  
 Abbott R., et al., 2021d, *The Astrophysical Journal Letters*, 913, L7  
 Abbott R., et al., 2021e, *The Astrophysical Journal*, 923, 14  
 Abbott R., et al., 2023a, *Phys. Rev. X*, 13, 041039  
 Abbott R., et al., 2023b, *Astrophys. J. Suppl.*, 267, 29

Bahaadini S., Rohani N., Coughlin S., Zevin M., Kalogera V., Katsagelos A. K., 2017, Deep Multi-view Models for Glitch Classification ([arXiv:1705.00034](https://arxiv.org/abs/1705.00034))  
 Basak S., Ganguly A., Haris K., Kapadia S., Mehta A. K., Ajith P., 2022, *The Astrophysical Journal Letters*, 926, L28  
 Cavaglia M., Staats K., Gill T., 2019, *Communications in Computational Physics*, 25  
 Chatterji S., Blackburn L., Martin G., Katsavounidis E., 2004, *Classical and Quantum Gravity*, 21, S1809  
 Cheung D. H. T., Rinaldi S., Toscani M., Hannuksela O. A., 2023, Mitigating the effect of population model uncertainty on strong lensing Bayes factor using nonparametric methods ([arXiv:2308.12182](https://arxiv.org/abs/2308.12182))  
 Choudhary S., More A., Suyamprakasam S., Bose S., 2023, *Phys. Rev. D*, 107, 024030  
 Collaboration T. L. S., et al., 2023, Search for gravitational-lensing signatures in the full third observing run of the LIGO-Virgo network ([arXiv:2304.08393](https://arxiv.org/abs/2304.08393))  
 Dai L., Venumadhav T., 2017, arXiv e-prints, [p. arXiv:1702.04724](https://arxiv.org/abs/1702.04724)  
 Dai L., Zackay B., Venumadhav T., Roulet J., Zaldarriaga M., 2020, arXiv e-prints, [p. arXiv:2007.12709](https://arxiv.org/abs/2007.12709)  
 Deguchi S., Watson W. D., 1986, *ApJ*, 307, 30  
 Deng J., Dong W., Socher R., Li L.-J., Li K., Fei-Fei L., 2009, in 2009 IEEE Conference on Computer Vision and Pattern Recognition. pp 248–255, [doi:10.1109/CVPR.2009.5206848](https://doi.org/10.1109/CVPR.2009.5206848)  
 Dodelson S., 2017, Gravitational lensing. Cambridge University Press  
 Ezquiaga J. M., Hu W., Lo R. K. L., 2023, *Phys. Rev. D*, 108, 103520  
 Fan X.-L., Liao K., Biesiada M., Piórkowska-Kurpas A., Zhu Z.-H., 2017, *Phys. Rev. Lett.*, 118, 091102  
 George D., Shen H., Huerta E. A., 2018, *Phys. Rev. D*, 97, 101501  
 Gong Y., Hou S., Liang D., Papantonopoulos E., 2018, *Phys. Rev. D*, 97, 084040  
 Goyal S., Haris K., Mehta A. K., Ajith P., 2021a, *Phys. Rev. D*, 103, 024038  
 Goyal S., D. H., Kapadia S. J., Ajith P., 2021b, *Phys. Rev. D*, 104, 124057  
 Gunn J. E., 1967, *ApJ*, 150, 737  
 Hannam M., Schmidt P., Bohé A., Haegel L., Husa S., Ohme F., Pratten G., Pürrer M., 2014, *Phys. Rev. Lett.*, 113, 151101  
 Hannuksela O. A., Haris K., Ng K. K. Y., Kumar S., Mehta A. K., Keitel D., Li T. G. F., Ajith P., 2019, *ApJ*, 874, L2  
 Haris K., Mehta A. K., Kumar S., Venumadhav T., Ajith P., 2018, arXiv e-prints, [p. arXiv:1807.07062](https://arxiv.org/abs/1807.07062)  
 Harris C. R., et al., 2020, *Nature*, 585, 357  
 Huang G., Liu Z., van der Maaten L., Weinberger K. Q., 2018, Densely Connected Convolutional Networks ([arXiv:1608.06993](https://arxiv.org/abs/1608.06993))  
 Jacobs C., Glazebrook K., Collett T., More A., McCarthy C., 2017, *Monthly Notices of the Royal Astronomical Society*, 471, 167  
 Jacobs C., et al., 2019, *The Astrophysical Journal Supplement Series*, 243, 17  
 Jaelani A. T., More A., Wong K. C., Inoue K. T., Chao D. C. Y., Premadi P. W., Cañameras R., 2023, Survey of Gravitationally lensed Objects in HSC Imaging (SuGOHI) – X. Strong Lens Finding in The HSC-SSP using Convolutional Neural Networks ([arXiv:2312.07333](https://arxiv.org/abs/2312.07333))  
 Jana S., Kapadia S. J., Venumadhav T., Ajith P., 2023, *Phys. Rev. Lett.*, 130, 261401  
 Janquart J., Hannuksela O. A., Haris K., Broeck C. V. D., 2022a, GOLUM: A fast and precise methodology to search for, and analyze, strongly lensed gravitational-wave events ([arXiv:2203.06444](https://arxiv.org/abs/2203.06444))  
 Janquart J., More A., Van Den Broeck C., 2022b, *Mon. Not. Roy. Astron. Soc.*, 519, 2046  
 Janquart J., et al., 2023, *Monthly Notices of the Royal Astronomical Society*, 526, 3832  
 Khan S., Husa S., Hannam M., Ohme F., Pürrer M., Forteza X. J., Bohé A., 2016, *Phys. Rev. D*, 93, 044007  
 Kormann R., Schneider P., Bartelmann M., 1994, *A&A*, 284, 285  
 Krizhevsky A., Sutskever I., Hinton G., 2012, *Neural Information Processing Systems*, 25  
 LIGO Scientific Collaboration Virgo Collaboration KAGRA Collaboration 2018, LVK Algorithm Library - LALSuite, Free software (GPL), [doi:10.7935/GT1W-FZ16](https://doi.org/10.7935/GT1W-FZ16)

- Lai K.-H., Hannuksela O. A., Herrera-Martín A., Diego J. M., Broadhurst T., Li T. G. F., 2018, *Phys. Rev. D*, 98, 083005
- LeCun Y., Bengio Y., Hinton G., 2015, *Nature*, 521, 436
- Li S.-S., Mao S., Zhao Y., Lu Y., 2018, *Monthly Notices of the Royal Astronomical Society*, 476, 2220
- Li Y., Fan X., Gou L., 2019, *The Astrophysical Journal*, 873, 37
- Li R., et al., 2021, *ApJ*, 923, 16
- Lo R. K., Magaña Hernandez I., 2023, *Physical Review D*, 107
- Macleod D. M., Areeda J. S., Coughlin S. B., Massinger T. J., Urban A. L., 2021, *SoftwareX*, 13, 100657
- Magare S., Kapadia S. J., More A., Singh M. K., Ajith P., Ramprakash A. N., 2023, *The Astrophysical Journal Letters*, 955, L31
- Maggiore M., et al., 2020, *Journal of Cosmology and Astroparticle Physics*, 2020, 050
- Miller M. C., Yunes N., 2019, *Nature*, 568, 469
- More A., More S., 2022, *Monthly Notices of the Royal Astronomical Society*, 515, 1044
- Nakamura T. T., 1998, *Phys. Rev. Lett.*, 80, 1138
- Ng K. K. Y., Wong K. W. K., Broadhurst T., Li T. G. F., 2018, *Phys. Rev. D*, 97, 023012
- Nitz A., et al., 2024, gwastro/pycbc: v2.3.3 release of PyCBC, doi:10.5281/zenodo.10473621, <https://doi.org/10.5281/zenodo.10473621>
- Oguri M., 2018, *Monthly Notices of the Royal Astronomical Society*, 480, 3842
- Oguri M., Takahashi R., 2020, *The Astrophysical Journal*, 901, 58
- Oost J., Mukohyama S., Wang A., 2018, *Phys. Rev. D*, 97, 124023
- Reitze D., et al., 2019, Bulletin of the AAS, 51
- Schmidhuber J., 2015, *Neural Networks*, 61, 85
- Schneider P., Ehlers J., Falco E. E., 1992, *Gravitational Lenses*. Springer, Berlin, Heidelberg
- Schutz B., 2009, *A First Course in General Relativity*, 2 edn. Cambridge University Press, doi:10.1017/CBO9780511984181
- Sereno M., Jetzer P., Sesana A., Volonteri M., 2011, *Monthly Notices of the Royal Astronomical Society*, 415, 2773
- Shen H., George D., Huerta E. A., Zhao Z., 2019, in ICASSP 2019 - 2019 IEEE International Conference on Acoustics, Speech and Signal Processing (ICASSP). IEEE, doi:10.1109/icassp.2019.8683061, <https://doi.org/10.1109/icassp.2019.8683061>
- Singer L. P., Price L. R., 2016, *Phys. Rev. D*, 93, 024013
- Singer L. P., Goldstein D. A., Bloom J. S., 2019, The Two LIGO/Virgo Binary Black Hole Mergers on 2019 August 28 Were Not Strongly Lensed (arXiv:1910.03601)
- Smith R., Field S. E., Blackburn K., Haster C.-J., Pürrer M., Raymond V., Schmidt P., 2016, *Phys. Rev. D*, 94, 044031
- Takahashi R., Nakamura T., 2003, *The Astrophysical Journal*, 595, 1039
- Virtanen P., et al., 2020, *Nature Methods*, 17, 261
- Wang Y., Stebbins A., Turner E. L., 1996, *Phys. Rev. Lett.*, 77, 2875
- Wei J.-J., et al., 2017, *Journal of Cosmology and Astroparticle Physics*, 2017, 035
- Wes McKinney 2010, in Stéfan van der Walt Jarrod Millman eds, Proceedings of the 9th Python in Science Conference. pp 56 – 61, doi:10.25080/Majora-92bf1922-00a
- Xu F., Ezquiaga J. M., Holz D. E., 2022, *The Astrophysical Journal*, 929, 9
- Yosinski J., Clune J., Bengio Y., Lipson H., 2014, How transferable are features in deep neural networks? (arXiv:1411.1792)
- Zaborowski E. A., et al., 2023, *ApJ*, 954, 68
- Çalışkan M., Ji L., Cotesta R., Berti E., Kamionkowski M., Marsat S., 2023a, *Phys. Rev. D*, 107, 043029
- Çalışkan M., Ezquiaga J. M., Hannuksela O. A., Holz D. E., 2023b, *Phys. Rev. D*, 107, 063023
- Çalışkan M., Anil Kumar N., Ji L., Ezquiaga J. M., Cotesta R., Berti E., Kamionkowski M., 2023c, *Phys. Rev. D*, 108, 123543

This paper has been typeset from a  $\text{\LaTeX}$  file prepared by the author.